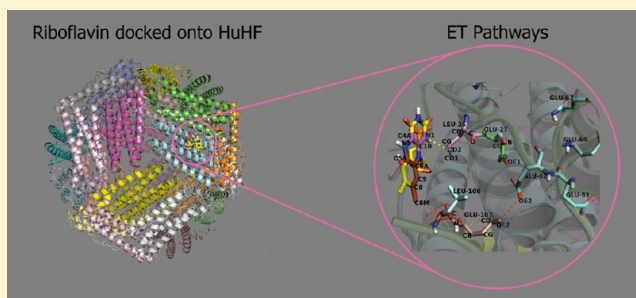


A Molecular Dynamics and Computational Study of Ligand Docking and Electron Transfer in Ferritins

Vijaya Subramanian and Deborah G. Evans*

The Nanoscience and Microsystems Program and the Department of Chemistry and Chemical Biology, University of New Mexico, Albuquerque, New Mexico

ABSTRACT: The mechanism of the reductive release of iron from the cavity of the iron storage protein, ferritin, has been difficult to confirm on the molecular level using experimental studies. In this paper, we use a variety of computational tools to study the binding of flavin redox agents to the protein surface, and the subsequent electron transfer (ET) through the protein coat. Flavin binding sites are identified that represent efficient routes to reduction of Fe(III) across the protein coat in human and bacterial ferritins. Using the pathways model and Dutton's packing density model, we show that ET across the protein coat to nucleation sites is feasible. Different protein configurations for human heavy and light chain ferritin were obtained along classical molecular dynamics trajectories and used for flavin binding and ET studies. We find that protein configuration affects both the binding and ET rate constants significantly. We show that the maximum possible ET rate constants to the nucleation site GLU-61 in human heavy chain ferritin for protein configurations along a MD simulation trajectory can differ by about 8 orders of magnitude compared to the crystal structure and in human light-chain ferritin rate constants vary by about 4 orders of magnitude.



I. INTRODUCTION

Ferritin is an iron storage protein found in eukaryotes and prokaryotes. It performs an important role in regulating iron levels in the different organisms as well as protecting against radical damage via, for example, the Fenton reaction.^{1–4} The crystal structures of mammalian, plant, and bacterial ferritins have been determined and reveal a wealth of information regarding structure/function relationships in the uptake and release of iron. Ferritins isolated from the various organisms, with a few exceptions, all consist of 24 protein subunits which together form a stable, hollow structure with 432 symmetry. The crystal structure of human heavy-chain ferritin (HuHF) is shown in Figure 1.⁵ The internal diameter of the structure is approximately 80 Å and outer diameter is 120 Å. The protein coat is thus about 20 Å thick. Two types of pores stud the protein surface. The pores along the eight 3-fold axes are lined with ASP and GLU residues. The pores along the six 4-fold axes are hydrophobic and in HuHF, four histidine residues form a ring on the cavity side. The parts of the protein exposed to solvent are lined with hydrophilic residues, particularly the acidic residues ASP and GLU. Several acidic residues are also found on the inner surface of the protein. Each protein subunit consists primarily of a 4-helix bundle (Figure 2a). The nonhelix regions in each subunit include loops at the N- and C-terminals and the AB turn and CD turn. There is a short extra helix E at the end of the D helix. In addition, a long loop BC connects helix B and helix C. This results in a 4-helix bundle with an up–down–down–up configuration. The BC loop participates in intersubunit interactions.

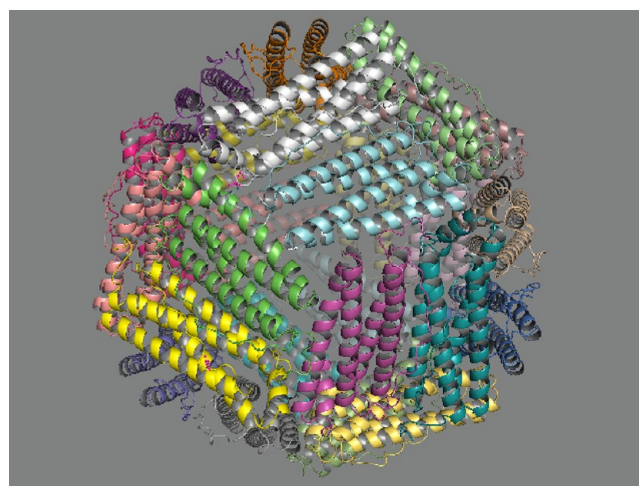


Figure 1. Human heavy-chain ferritin (HuHF): 24 identical 4-helix bundles enclose a cavity. Two types of pores are present in the protein. The pore with 3-fold symmetry is visible in the figure.

There are two kinds of subunits present in mammalian ferritin, the heavy chain and the light chain. The heavy chains contain a ferroxidase site within the 4-helix bundle that catalyzes the oxidation of Fe(II) to Fe(III).⁶ There are seven conserved residues in this region which bind two iron atoms

Received: February 1, 2012

Revised: June 6, 2012

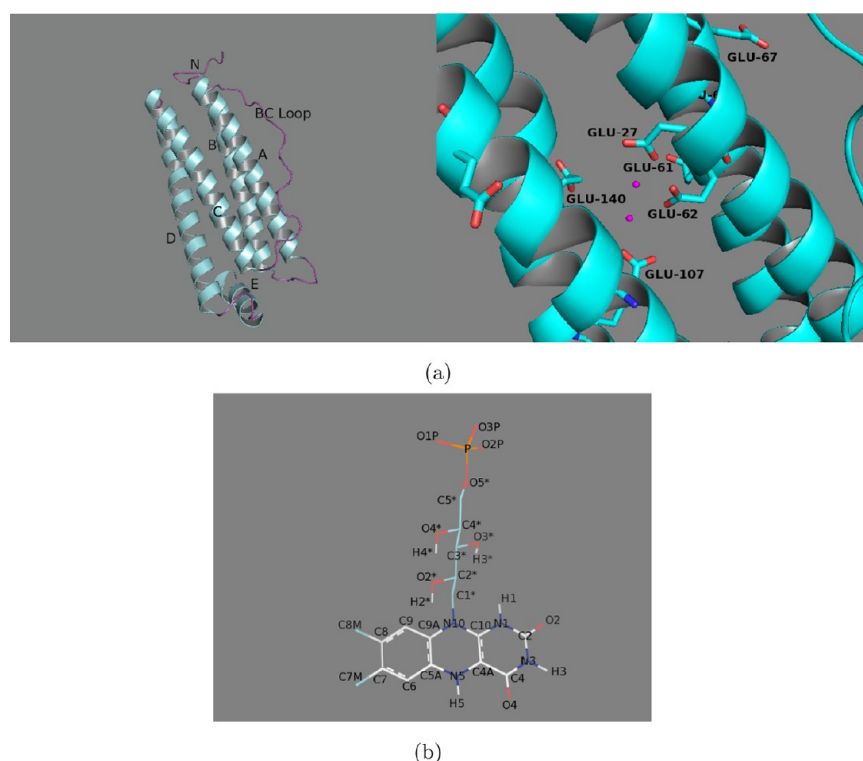


Figure 2. (a) On the left, one subunit from HuHF(2fha). The up–down–down–up form of the 4-helix bundle is evident. The figure on the right shows the ferroxidase site in greater detail. The possible location of Fe(II) is shown in magenta. (b) Reduced flavin mononucleotide (FMNH₂). Reduced riboflavin (RBFH₂) has a hydrogen in the place of the phosphate group.

(Figure 2a). Light-chain ferritin does not possess a ferroxidase site and is thought to play a role in iron biomineralization.^{4,5} Bacterioferritin similarly has 432 symmetry and 24 identical subunits each possessing a ferroxidase center.⁷ In addition, 12 heme molecules are located along the 2-fold symmetry axis between two adjacent subunits (Figure 3a,b). The role of the heme molecules is not known, but they are thought to participate in reduction of Fe(III).⁸

The mechanism of iron storage and release has been studied by various researchers. Current opinion is that the ferroxidase site is responsible for the oxidation of Fe(II) to Fe(III) via a peroxo intermediate.^{1,9} Light-chain ferritin also incorporates Fe(III) independently of the heavy chain, so there must be an additional route for the deposition of Fe(III) within the LC ferritins. The oxidized Fe then moves into the cavity and core formation is thought to originate at nucleation sites on the inner surface of the protein.⁴

Very little is known of the mechanism of iron release *in vivo*. Studies have shown that both reducing agents and iron chelators can effect iron release from ferritin *in vitro*. The chelators are in general found to release iron very slowly, at rates that are not of physiological significance.^{2,10} In the presence of urea (10 mM) or at low pH, chelators like benzhydroxamic acid were found to release iron at faster rates.¹¹ Other researchers have indicated that agents such as urea (1–10 mM) or peptides, selected from a combinatorial library for binding near the 3-fold pore, induce pore opening and enhance Fe(II) release under reductive conditions. They suggest that such “pore gating” mechanisms may exist *in vivo* for timely release of iron when needed.^{12–14} Yet other researchers claim that the lysosome which completely denatures the ferritin molecule is the site of Fe(III) reduction and release in the cytosol.¹⁵

Reducing agents like dihydriboflavin (RBFH₂), dihydroflavin mononucleotide (FMNH₂)¹⁶ (Figure 2b), and flavoproteins¹⁷ have been found to be very effective in iron release from ferritin. The mechanism of reduction is not very clear. It is unknown at this point whether reducing agents enter the ferritin cavity and directly react with Fe(III) or effect reduction via electron transfer mediated by the protein coat. An early paper by Jones et al.¹⁸ suggests that reduced flavins diffuse into the ferritin cavity where direct electron transfer from the flavins to Fe(III) occurs. They deduce this from the fact that RBFH₂ immobilized by binding to sepharose is ineffective as a reducing agent for iron trapped inside the ferritin protein core but reduces protein free synthetic Fe(III) cores generated by precipitation from basic hydrolysis of ferric citrate at rates that are 20% that of reduction by free RBFH₂. This observation could also mean that the immobilized RBFH₂ cannot adopt the right conformation for binding to the ferritin surface to effect electron transfer. Work done by Chasteen et al. showed that small molecules such as nitroxide radicals are able to diffuse into the protein cavity but with half-lives of about 60 min.¹⁹ They argue that the half-lives for larger flavins to diffuse into the ferritin cavity would be much greater and hence make this route to reduction physiologically irrelevant. For example, it takes RBFH₂ just 15 min to reduce Fe(III) completely *in vitro*.¹⁶ In work done by Watt et al. to address the question of iron release, *Azotobacter vinelandii* flavodoxin and *Azotobacter vinelandii* flavoprotein were both used as the reducing agents.¹⁷ Both proteins are large and contain cofactors which are not thought to be released during catalysis. As it is not probable that either protein enters the cavity, Fe(III) reduction is most likely to take place via protein–protein binding followed by electron transfer across the protein coat.

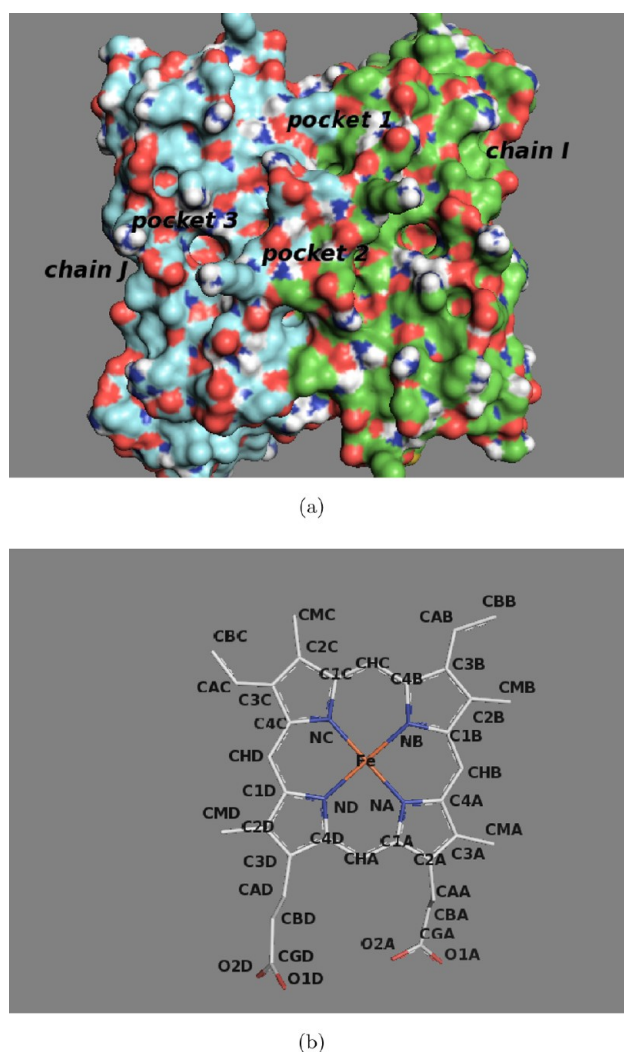


Figure 3. (a) Two subunits from 1BCF. The pockets 1, 2, and 3 on the surface are highlighted. The heme molecule, not visible here, is located directly below pocket 2. The ferroxidase site is located near pocket 3. (b) The heme molecule.

In this paper, we use molecular simulation tools to identify possible mechanisms for the release of iron from the ferritin core. Experimental work does not provide conclusive evidence as to whether it is essential for reducing agents to enter the ferritin cavity to effect reduction of Fe(III). Since simulation tools can provide key mechanistic insights at the atomistic level, we specifically examine a number of questions that are related to the feasibility of electron transfer across the protein coat from bound reducing agents such as RBFH2 and FMNH2. For reducing agents to be effective without entering the core, electron transfer across the protein coat would have to proceed at a reasonable rate. This computational study therefore focuses on three major issues: (1) identifying potential binding sites on the outer surface of the protein for the reducing agents; (2) determining electron-transfer rate constants and possible pathways across the protein coat; and (3) determining how significantly binding events and electron-transfer pathways and rate constants vary due to changes in the protein conformation.

In section II of the paper, we use classical molecular dynamics (MD) simulations to sample protein conformations in solution. Starting with the ferritin crystal structures, we use classical MD to generate trajectories up to several hundred

nanoseconds. Specific configurations (or protein conformations) at different time steps along these MD trajectories are used in docking and electron-transfer calculations discussed in the subsequent sections of the paper. In section III of the paper, the docking modeling program, Autodock, is used to identify potential sites for dihydroflavin binding to the ferritins: human heavy-chain ferritin (HuHF), human light-chain ferritin (HuLF), and bacterioferritin (1BCF), in the crystal structure conformation and for different ferritin configurations along MD simulation trajectories. The results from these docking calculations are then used as the starting point for computational studies of electron-transfer processes across the protein coat. In section IV, rate constants for electron transfer across the protein coat from the bound dihydroflavins to putative iron nucleation sites as well as the ferroxidase site are determined. Electron transfer to the heme in bacterioferritin is also studied. Electron transfer through the ferritin shell is examined using two computational approaches commonly used for electron transfer through biological systems and proteins, namely, the pathways model²⁰ and Dutton's average packing density model.²¹

II. MOLECULAR DYNAMICS SIMULATION

The crystal structures of the apoferritins chosen for the simulation were obtained from the protein data bank: 2FHA for the human heavy-chain ferritin and 2FFX for the human light-chain ferritin. The two proteins were simulated independently according to the procedures described. The MD simulation was performed using the GROMACS simulation package.^{22,23} The GROMOS-96 43a1 force field was used.²⁴ The water of crystallization and calcium ions were removed from the crystal structure prior to simulation. The protein was then solvated with explicit water. The simple point charge (SPC) model was used to represent the water molecules. Sodium ions were then added to balance the charges in the system. The solvated system was first subjected to energy minimization using the steepest descent method. This was followed by position restrained MD simulation where the protein position was restrained and the solvent allowed to relax. The particle mesh Ewald method was used to calculate electrostatic interactions. The temperature was fixed at 310.15 K. This was followed by equilibration under NPT conditions. The Berendsen thermostat and barostat were used to maintain temperature and pressure constant. Hydrogen bond constraints were applied and a time step of 2 fs was implemented. The solvated, equilibrated protein HuHF was then simulated for 216 ns and HuLF for 20 ns. The MD simulations provide a method of sampling the conformations of ferritin in solution. In subsequent studies, ferritin configurations along these MD trajectories are used as the starting point for examining binding and electron-transfer events. The MD simulation provides a set of configurations that can be used to study experimentally measurable quantities for ferritin conformations beyond the crystal structures.

III. COMPUTATIONAL STUDY OF FLAVIN DOCKING

It is known that 4-helix bundles in several proteins have active sites located at the interface of the two interior helices.²⁵ As we were primarily interested in locating sites on the surface of ferritin which would afford effective electron transfer to the iron core, sites close to the putative nucleation sites were chosen for the docking studies. The iron binding ferroxidase site was also considered. The crystal structures chosen for this study have

the specific PDB IDs: 2FHA for the human heavy-chain ferritin, 2FFX for the human light-chain ferritin, and 1BCF for the bacterioferritin. Visual inspection of the molecular surface using the visualization program PyMOL²⁶ and also the pocket search algorithm CastP²⁷ showed the presence of pockets both on the outer and inner surface of the 4-helix bundle near the ferroxidase site of HuHF. These are more pronounced in HuHF after several nanoseconds of MD simulation. In HuLF there is a pocket offset from the center of the 4-helix bundle but located over the nucleation sites. In 1BCF, three different pockets were chosen according to their proximity to the heme group located in the interior of the protein. The molecular docking calculations are intended to give insight into binding as well as the effectiveness of electron transfer across the protein coat from these sites. Flavins were chosen in this study as they are physiologically relevant molecules, often found as cofactors in redox proteins. The two flavoproteins, *Azotobacter vinelandii* flavodoxin and *Azotobacter vinelandii* flavoprotein, have been found to be effective reducing agents in the release of iron from ferritin in vitro.¹⁷ RBFH2 and FMNH2 are known to effect reduction of ferritin iron on physiologically relevant time scales. The rate constants for Fe(III) release from horse spleen ferritin by FMNH2 and RBFH2 were found to be (when modeled as a second-order reaction) at 10.8 and 13.0 M⁻¹ s⁻¹, respectively.¹⁶ Saturation kinetics has also been observed with respect to the flavin concentration¹⁸ and may be indicative of flavin–ferritin complex formation. The reduced flavin structure was obtained from HIC-UP heterocompound information center under residue id FNR.²⁸

We used the docking program AutoDock²⁹ to find potential binding sites on the outer surface of HuHF, HuLF, and 1BCF. This freeware uses the Lamarckian genetic search algorithm and a free-energy based scoring function to determine the ligand binding energy. The scoring function includes van der Waals interactions, hydrogen-bonding interactions, torsion terms, electrostatic interactions, and a desolvation term. The Autodock algorithm provides sufficient accuracy to discriminate between leads with milli-, micro-, and nanomolar inhibition constants.³⁰ Gasteiger partial charges were assigned to both protein and ligand for calculating the electrostatic interaction terms. A total charge of −2 was assigned to the phosphate group in FMNH2. A large grid was centered around the pockets near the nucleation sites seen by inspection of the molecular surface for each docking simulation. The genetic algorithm input parameters of a maximum of 2 500 000 energy evaluations or 27 000 generations for each run were used and a hundred separate runs were carried out for each ligand–protein combination. Default values were used for all other input parameters. One hundred docking runs were carried out in each case and the resulting docked structures were clustered with a 2 Å tolerance for the rmsd. In most cases, the docked structures represent conformations from one of the larger clusters.

III.A. Docking in HuHF. Docking to HuHF is studied for the crystal structure conformation and several protein configurations taken as snapshots along the MD simulation trajectory. The free energy of binding and the inhibition constants for the various docked structures of RBFH2 and FMNH2 centered around the central part of the 4-helix bundle are given in Table 1. We found that RBFH2 and FMNH2 bind differently to the crystal structure. The amino acid residues within 5 Å of the docked flavin structures are highlighted in Figures 4 and 5. In both cases the residues involved in binding are ARG-22, GLU-116, LEU-26, ASN-25, TYR-29, ASN-109,

Table 1. Binding Energy and Inhibition Constants for RBFH2 and FMNH2 Docked on the Crystal Structure of HuHF and Configurations from Different Time Steps of the MD Trajectory

HuHF snapshot confign	RBFH2		FMNH2	
	binding energy (kcal mol ⁻¹)	inhibition const (mM)	binding energy (kcal mol ⁻¹)	inhibition const (mM)
crystal	−5.5	0.1	−2.3	22
8.6	−3.9	1.5	−3.6	2.4
126	−4.5	0.5	−4.1	1.1
216	−3.2	4.3	−3.5	2.7

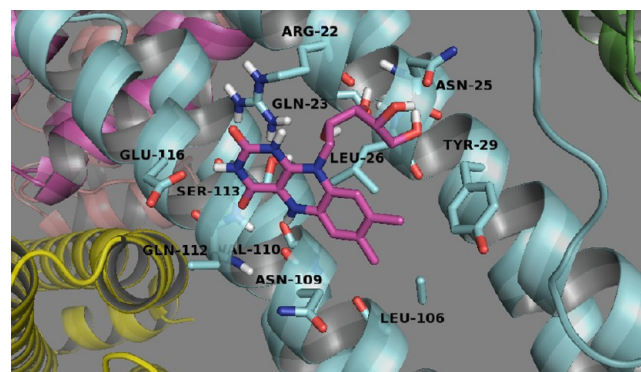


Figure 4. RBFH2 docked near the diiron center of the crystal structure of HuHF. All residues within 5 Å of the docked structure are highlighted. ARG-22, TYR-29, LEU-26, and SER-23 among other residues are found to interact with RBFH2.

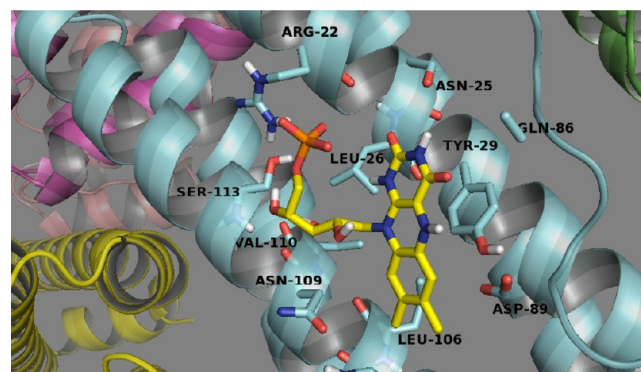


Figure 5. FMNH2 docked near the diiron center of the crystal structure of HuHF. All residues within 5 Å of the docked structure are highlighted. As in the case of RBFH2, ARG22, LEU-26, TYR-29, and SER-111 have favorable interactions with FMNH2. The phosphate group is associated with ARG-22.

and VAL-110 and LEU-106. The orientation of the isoalloxazine rings, though, is very different for the two flavins. In the case of RBFH2 the isoalloxazine ring is oriented toward ARG-22 and in the case of FMNH2 the charged phosphate group interacts with ARG-22. RBFH2 has five hydrogen-bonding interactions with the protein—the isoalloxazine N3H- (GLU-116), N1H- (ARG-22), N5H- (ASN-109), and the ribose OH5* and OH4*-(ASN-25). FMNH2 has only one hydrogen-bonding interaction between the phosphate group and ARG-22. In both cases the N5 electron donor atom of the isoalloxazine ring is oriented away from the center of the helix bundle. The

inhibition constant, K_i , for the two docked structures is 0.1 mM for RBFH2 and 22 mM for FMNH2.

At 8.6 ns along the MD trajectory, the docked structures (Figure 6) are found to be quite different compared to that with

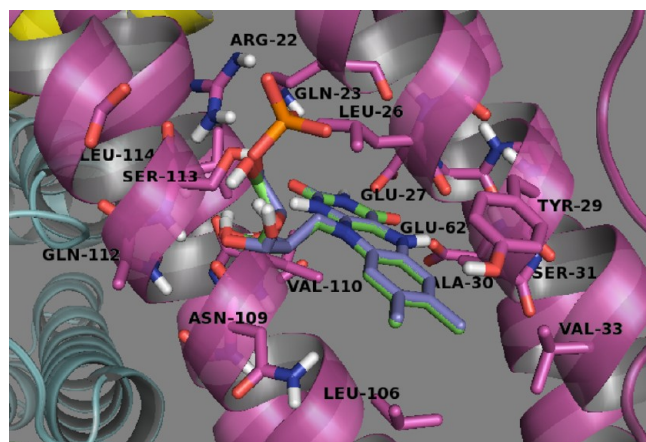


Figure 6. RBFH2 and FMNH2 docked on the same subunit as in Figure 4 after 8.6 ns of MD simulation. All residues within 6 Å of the docked structure are highlighted. GLU-27 and GLU-62 are in closer proximity to the docked ligand. LEU-26, LEU-106, and TYR-29 have rotated away from the interhelical region making the cavity larger than in the crystal structure. The isoalloxazine ring is oriented toward the interior.

the crystal structure (Figure 5). LEU-26, LEU-106, and TYR-29 have rotated away from the interhelical region, making the cavity larger than in the crystal structure. The docked structures for both RBFH2 and FMNH2 have their isoalloxazine rings oriented toward the interior of the 4-helix bundle. The ribose chain in both are oriented in a similar fashion, with the phosphate moiety of FMNH2, in particular, directed toward the ARG-22. The electron-transfer donor N5 atom of the isoalloxazine ring of the flavins can be seen close to GLU-27 and GLU-62, residues known to bind iron. While residues that are within 6 Å of the flavins remain the same as in the case of binding to the crystal structure, the orientations are very different. TYR-25 is located near the dimethyl-substituted ring of the flavin. RBFH2 forms one hydrogen bond between the isoalloxazine N3H and GLU-27. FMNH2 forms three hydrogen bonds, N3H-GLU-27, and two phosphate-ARG-22 hydrogen bonds. The inhibition constants for the RBFH2 and FMNH2 docked structures are 0.1 and 1.5 mM, respectively.

For the configuration taken at 126 ns along the simulation trajectory, the docked structure for RBFH2 does not overlap the docked structure for FMNH2 as closely (Figures 7 and 8). While the amino acids involved in close interactions with the flavins remain the same, the N5–H bond of the isoalloxazine rings is not pointing into the middle of the helix bundle as the ring is tilted away from the bundle. The N3H-(GLU-27) hydrogen bond persists in these docked structures. RBFH2 forms two additional hydrogen bonds between the ribose hydroxyls and ARG-22. FMNH2 forms four additional hydrogen bonds, two between the ribose hydroxyls and ASN-111 and GLN-23, and two hydrogen bonds between the phosphate group and ARG-22. At 156 ns the position of the isoalloxazine ring is shifted and the N5H hydrogen bonds to the carbonyl oxygen of GLU-27. The N3H hydrogen bond to GLU-27 is not observed (Figure 9). The inhibition constants for RBFH2 and FMNH2 are 0.3 and 1.9 mM respectively.

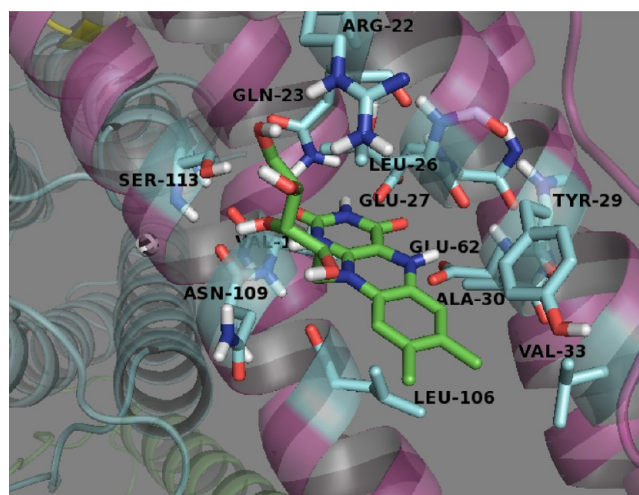


Figure 7. RBFH2 docked on the same subunit as in Figure 4 after 126 ns of MD simulation. All residues within 5 Å of the docked structure are highlighted. Interactions remain similar though GLU-27 and GLU-62 have moved toward the cavity.

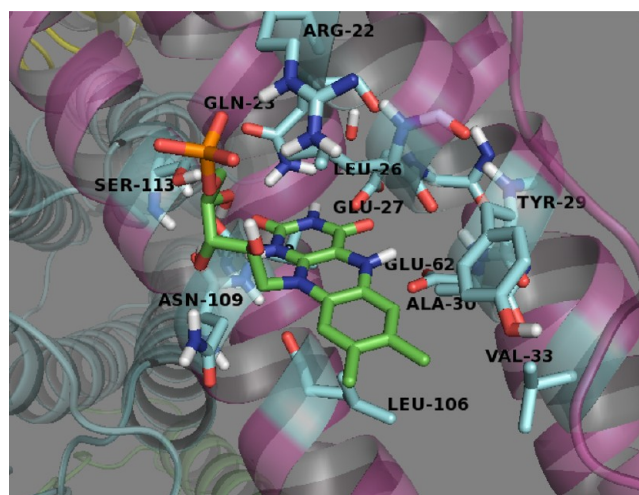


Figure 8. FMNH2 docked on the same subunit as in Figure 4 after 126 ns of MD simulation. All residues within 5 Å of the docked structure are highlighted. The phosphate group interacts with ARG-22 which is now oriented toward the interhelical region.

By 216 ns the N5H of the isoalloxazine in the docked structures is within hydrogen-bonding distance of GLU-27 (Figure 10). The isoalloxazine ring is oriented directly toward the interior of the cavity. The distances between the N5 donor atom of RBFH2 and the carboxylate oxygen of the ferroxidase site glutamic acids GLU-27, GLU-61, and GLU-62 reduced from 9.1, 19.4, and 11.3 Å in the crystal structure to 2.8, 13.5, and 5.7 Å after 216 ns of simulation, respectively. Helix A and helix C have moved apart and helix B and helix D have moved inward (Figure 11). In all the docked structures, the phosphate group of FMNH2 is associated with ARG-22. ARG-22 is a conserved residue in most of the ferritins mentioned in Hempstead's paper.⁵ In addition, TYR-29 is observed to be associated with the isoalloxazine moiety in all the docked structures. The ribose side chain of RBFH2 on the other hand adopts more varied orientations. In Figure 12, four of the residues associated with the docked flavins are displayed at the different simulation times. ARG-22 shows the most variation in

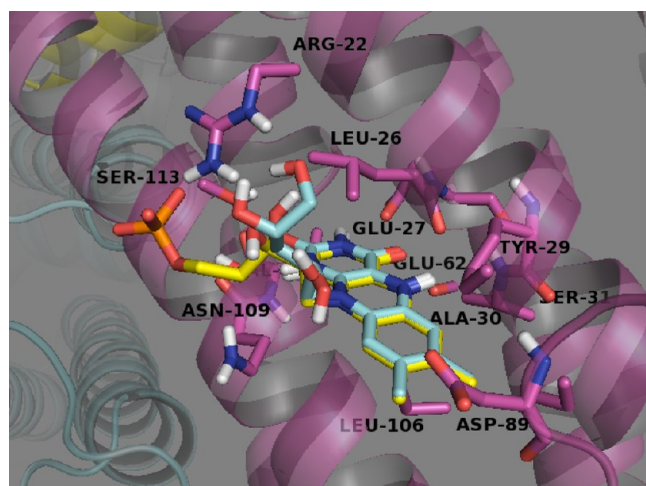


Figure 9. RBFH2 and FMNH2 docked on the same subunit as in Figure 4 after 156 ns of MD simulation. All residues within 6 Å of the docked structure are highlighted. ARG-22 side chain lies right across the two helices. The docked configuration is similar to that at 126 ns.

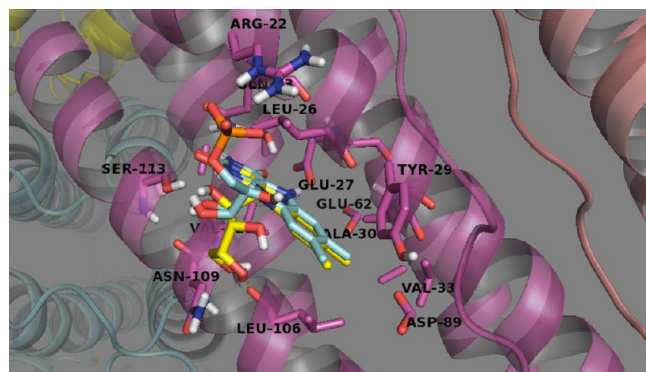


Figure 10. RBFH2 and FMNH2 docked on the same subunit as in Figure 4 after 216 ns of MD simulation. All residues within 6 Å of the docked structure are highlighted. The cavity is much more open than at the previous time steps. GLU-27 and GLU-62 have moved inward toward the cavity. GLU-27 is within hydrogen-bonding distance of the N5H of the isoalloxazine ring. ARG-22 is positioned away from the center of the helix bundle. The ribose groups of the two flavins are oriented differently. The phosphate group of FMNH2 interacts with ARG-22.

position followed by TYR-29. Side-chain positions fluctuate significantly within the picosecond–nanosecond time scale. Backbone motion is slower and is observed in the longer nanosecond (>10 ns) time scale. The backbone relaxation as well as side-chain movement appear to have a significant effect on the orientation of the binding. The inhibition constants for RBFH2 and FMNH2 are found to be 4.3 and 2.7 mM, respectively, by 216 ns. Interestingly, the experimental data also suggest that the inhibition constants must be greater than 1 mM.¹⁸

III.B. Docking in HuLF. The human light-chain ferritin, HuLF, does not possess ferroxidase activity as GLU-62 in HuHF is replaced by LYS-62 in HuLF which forms a salt bridge with GLU-107.^{5,31} It is, however, presumed to have nucleation sites at the following residues: GLU-57, GLU-60, GLU-61, and GLU-64. Pockets on the surface that were closest to the nucleation sites were chosen for the docking runs. Docked configurations of RBFH2 and FMNH2 were obtained for the

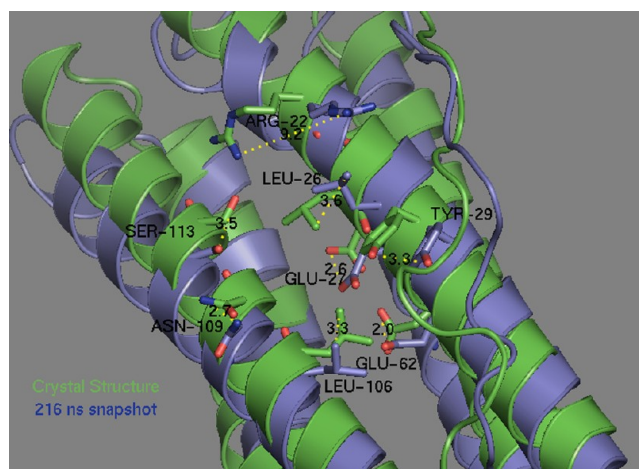


Figure 11. Difference between the crystal structure of ferritin and the structure after 216 ns of simulation is shown in this figure. Helix C has rotated outward and the two residues GLU-27 and Glu-62 are closer to the outer surface of the protein after 216 ns of simulation.

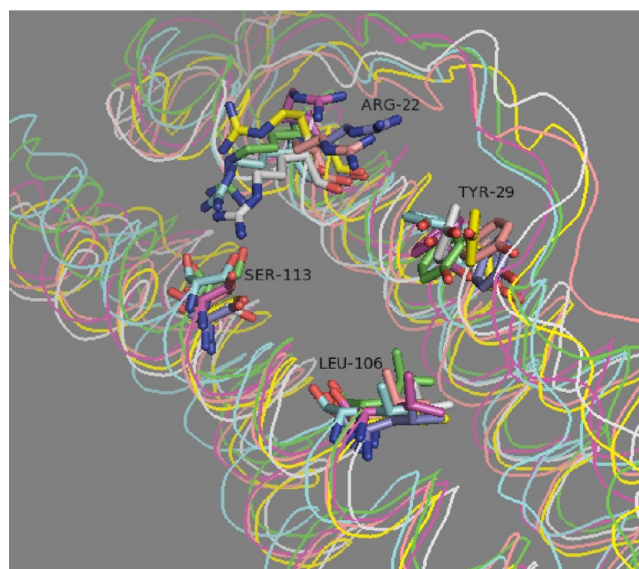


Figure 12. Side chains that were identified as important from the docking calculations at the various time steps, including the crystal structure, are shown. The time steps were chosen at random and the different positions adopted by the side chains is evident. ARG-22 shows the most variation in position and to a lesser extent Tyr-29.

crystal structure, and the 10 and 20 ns snapshots from the MD simulation.

The inhibition constants for RBFH2 and FMNH2 docked on the crystal structure are fairly low at 0.05 and 0.02, respectively (Table 2). The residues involved in RBFH2 binding are LYS-86, LYS-109, GLN-29, LEU-26, and ALA-89 (Figure 13). The first three residues interact with the ribose chain. The N3H of the isoalloxazine ring forms a hydrogen bond with THR-33. The isoalloxazine ring is oriented perpendicular to the helices. FMNH2 binds somewhat differently, with the phosphate group interacting with LYS-109 and LYS-86 (Figure 14). Two hydrogen bonds are observed between ALA-89 and LYS-109 and the carbonyl oxygens of the isoalloxazine ring. After 10 ns of simulation, the inhibition constants increase for both FMNH2 and RBFH2. The location of the binding pocket changes when compared to the crystal structure. The

Table 2. Binding Energy and Inhibition Constants for RBFH2 and FMNH2 Docked on the Crystal Structure of HuLF and Configurations from Different Time Steps of the MD Trajectory

HuLF snapshot confign	RBFH2		FMNH2	
	binding energy (kcal mol ⁻¹)	inhibition const (mM)	binding energy (kcal mol ⁻¹)	inhibition const (mM)
crystal	−5.9	0.05	−6.5	0.02
10	−5.0	0.2	−4.2	0.9
20	−4.4	0.6	−4.1	1.0

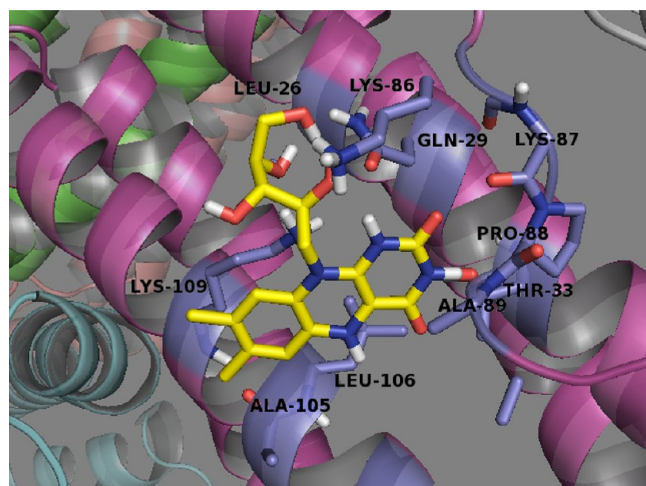


Figure 13. RBFH2 docked on the crystal structure of light chain ferritin (HuLF). All residues within 5 Å of RBFH2 are highlighted in gray-blue. The cavity is much smaller than in the case of HuHF. LYS-86, LEU-26, and GLN-29 interact with the ribose chain.

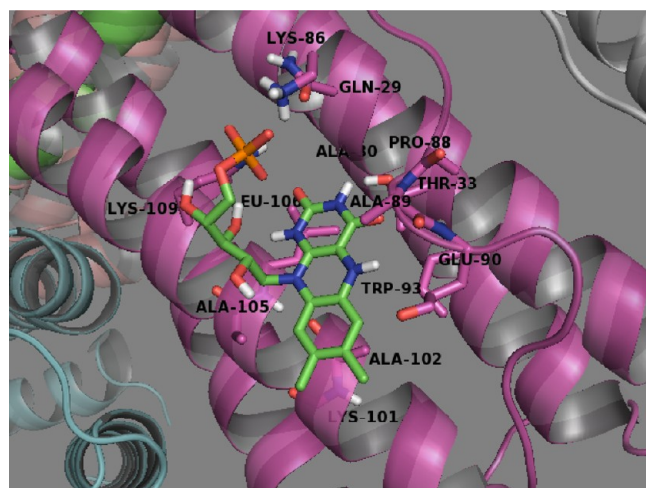


Figure 14. FMNH2 docked on the crystal structure of light-chain ferritin (HuLF). All residues within 5 Å of FMNH2 are shown. The isoalloxazine ring is oriented parallel and away from the cavity center. The phosphate group interacts with LYS-86.

isoalloxazine rings of both flavins lie in the same position within the pocket. LYS-86 points toward the middle of the helix bundle and LYS-109 has rotated away from the interhelical region (Figure 15). The phosphate group of FMNH2 is associated with LYS-86. The N5 position of the isoalloxazine ring is oriented toward helix A and forms a hydrogen bond with

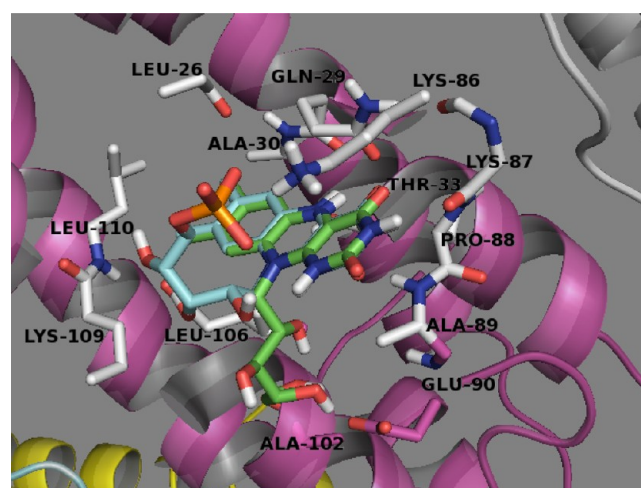


Figure 15. RBFH2 and FMNH2 docked on the 4-helix bundle of HuLF after 10 ns of simulation. Both flavins adopt similar conformation except for the ribose chains. The isoalloxazine ring is within the cavity and oriented toward helix A. The phosphate group of FMNH2 interacts with LYS-86.

GLN-29. For the configuration taken at 20 ns along the MD simulation trajectory, the inhibition constants are in the millimolar range. LYS-86 and LYS-109 are oriented away from the pocket and the isoalloxazine ring is oriented toward helix A (Figure 16). Two hydrogen bonds are observed in

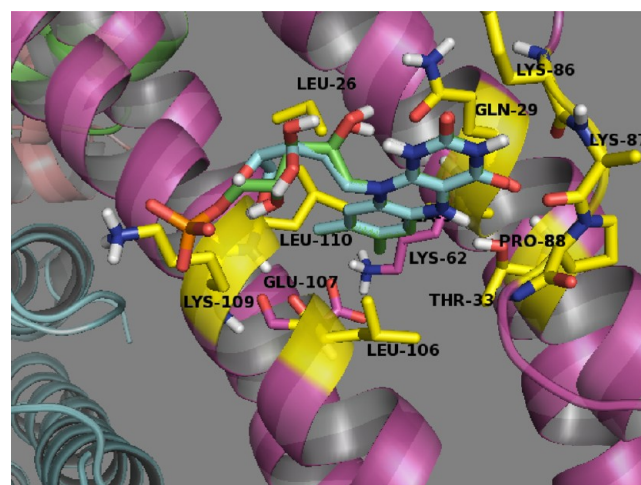


Figure 16. RBFH2 and FMNH2 docked on the 4-helix bundle of HuLF after 20 ns of simulation. The cavity is much more exposed with the BC loop moving away from the helix-bundle center. The isoalloxazine group is oriented toward helix A. The phosphate group of FMNH2 interacts with LYS-109.

RBFH2 binding, one between the NSH and THR-33 and the other between the ribose H2* and GLN-29. FMNH2 forms one hydrogen bond between N5–H and THR-33.

III.C. Docking in 1BCF. The heme molecule within the protein cavity is found to play an important role in iron release from bacterioferritin.³² In order to determine the possibility of electron transfer across the protein coat to the heme groups, flavin binding to the protein surface in the crystal structure of bacterioferritin (1BCF) was also studied. Three pockets on the outer surface with reasonable proximity to the heme molecule were chosen as potential binding sites for the flavins (Figure 3).

The docking results (Table 3) show that binding to pockets 1 and 2 is stronger while binding to pocket 3 near the ferroxidase site is in the millimolar range.

Table 3. Binding Energy and Inhibition Constants for RBFH2 and FMNH2 Docked on the Crystal Structure of 1BCF

1BCF	RBFH2		FMNH2	
	binding energy (kcal mol ⁻¹)	inhibition const (mM)	binding energy (kcal mol ⁻¹)	inhibition const (mM)
pocket 1	−5.5	0.09	−4.4	0.6
pocket 2	−5.7	0.06	−4.1	1.0
pocket 3	−4.1	1.1	−4.3	0.75

Binding to pocket 1 (Figure 17) shows the isoalloxazine ring of RBFH2 (blue) oriented away from the heme molecule and

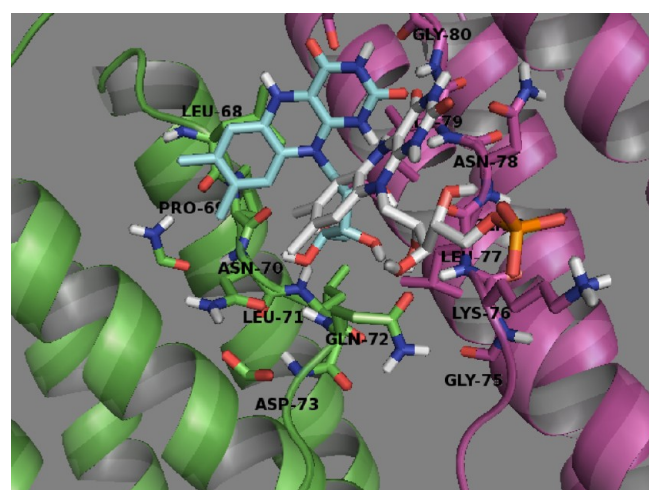


Figure 17. RBFH2 and FMNH2 docked within pocket 1, a possible site from which electron transfer to the heme group could occur. The isoalloxazine moiety of RBFH2 is oriented away from the heme. The phosphate group of FMNH2 interacts with LYS-76 and the isoalloxazine ring is oriented toward the interior of the pocket.

the ribose chain directed toward it. FMNH2 (white) is oriented differently with the ribose chain and phosphate group pointed in the direction of LYS-76 of chain I. Residues within 5 Å of the docked flavins are highlighted and include residues 68–73 on chain J and residues 75–80 on chain I. The residues are all located on the BC loop of the respective chains.

Pocket 2 in the crystal structure shows interesting symmetry and is located right on top of the heme molecule. Docking over this site with a grid large enough to cover the whole pocket shows two symmetrical binding orientations. One of the docked conformations is shown in (Figure 18) with the phosphate group of FMNH2 near LYS-76 of chain I. The other docked structure has the phosphate group of FMNH2 near LYS-76 of chain J. Residues within 5 Å of the docked structure are displayed in the figure. The isoalloxazine ring of both flavins sits parallel to the surface of the pocket and is not oriented toward the heme molecule. It is possible protein dynamics would allow a different more favorable orientation of the donor site for electron transfer.

In the case of binding to pocket 3, the BC loop is partially covering the ferroxidase site. The binding of the FMNH2 to this site is directed by LYS-76 of chain J (Figure 19) in addition

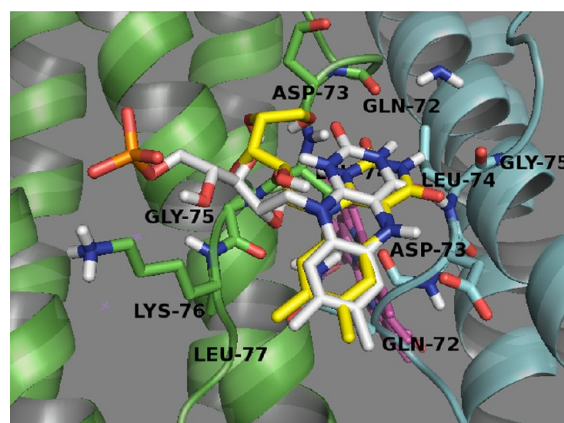


Figure 18. RBFH2 (yellow) and FMNH2 (white) docked over pocket 2. The heme group (pink) is located within BCF below pocket 2. The isoalloxazine moiety lies parallel to the cavity surface. The phosphate group of FMNH2 interacts with LYS-76.

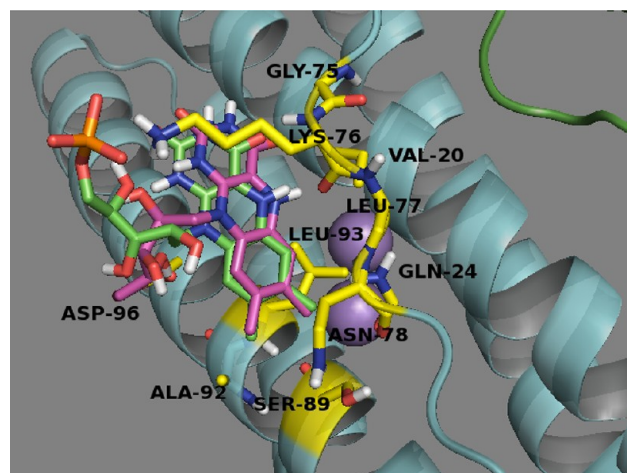


Figure 19. RBFH2 (pink) and FMNH2 (green) docked on pocket 3 located over the ferroxidase site in the 4-helix bundle of 1BCF. The cavity is partially covered by the BC loop. The phosphate group of FMNH2 interacts with LYS-76.

to LEU-93, ASN-78, GLY-75, and LEU-77 among others. In the case of HuHF and HuLF, side-chain and backbone motion affects the binding location and orientation and should be expected in 1BCF also; for example, with BC loop motion the ferroxidase site could become much more exposed.

IV. ELECTRON TRANSFER

IV.A. ET Models. Electron transfer was studied using both the pathways model^{20,33,34} and Dutton's average packing density model.²¹ In the pathways model of nonadiabatic electron transfer between donor and acceptor mediated by a bridge, the electron tunneling matrix element, H_{DA} , is proportional to the product of contributions from individual through bond, through hydrogen bond, and through space couplings, $H_{DA} \propto \prod_i \epsilon_{(i)}^{(c)} \prod_j \epsilon_{(j)}^{(hb)} \prod_k \epsilon_{(k)}^{(ts)}$. The coupling is highest for the covalent bond, $\epsilon^{(c)}$, and is less for the hydrogen bond, $\epsilon^{(hb)}$, and least for a through space jump, $\epsilon^{(ts)}$. Pathway couplings

$$T'_{DA} = \prod_i \epsilon_{(i)}^{(c)} \prod_j \epsilon_{(j)}^{(hb)} \prod_k \epsilon_{(k)}^{(ts)} \quad (1a)$$

Table 4. Pathway Coupling, T'_{DA} , Eq 1a, and Rate Constants, Eq 1b, for Electron Transfer from RBFH2 and FMNH2 Docked on the Crystal Structure of HuHF and Configurations at Different Time Steps of the MD Simulation^a

terminal glutamate	snapshot (ns)	RBFH2		FMNH2	
		T'_{DA}	rate const k_{et} (s ⁻¹)	T'_{DA}	rate const k_{et} (s ⁻¹)
GLU-27	crystal	6.3×10^{-5}	4.0×10^5	4.4×10^{-5}	1.9×10^5
GLU-61	crystal	3.2×10^{-8}	1.0×10^{-1}	4.4×10^{-8}	1.9×10^{-1}
GLU-62	crystal	3.1×10^{-6}	9.6×10^2	1.5×10^{-6}	2.2×10^2
GLU-27	8.6	1.1×10^{-2}	1.2×10^{10}	1.1×10^{-2}	1.2×10^{10}
GLU-61	8.6	2.5×10^{-5}	6.2×10^4	2.5×10^{-5}	6.2×10^4
GLU-62	8.6	7.0×10^{-3}	4.9×10^9	7.0×10^{-3}	4.9×10^9
GLU-27	126	1.6×10^{-2}	2.6×10^{10}	1.9×10^{-2}	3.6×10^{10}
GLU-61	126	5.7×10^{-6}	3.2×10^3	3.8×10^{-6}	1.4×10^3
GLU-62	126	1.6×10^{-3}	2.6×10^8	1.1×10^{-3}	1.2×10^8
GLU-27	156	1.6×10^{-2}	2.6×10^{10}	1.3×10^{-2}	1.7×10^{10}
GLU-61	156	9.7×10^{-6}	3.2×10^3	1.2×10^{-5}	1.4×10^3
GLU-62	156	2.7×10^{-3}	7.3×10^8	3.2×10^{-3}	1.0×10^9
GLU-27	216	5.3×10^{-2}	2.8×10^{11}	5.6×10^{-2}	3.1×10^{11}
GLU-61	216	1.8×10^{-6}	3.2×10^2	1.8×10^{-6}	3.2×10^2
GLU-62	216	4.9×10^{-4}	2.4×10^7	4.4×10^{-4}	1.9×10^7

^aThe terminal glutamate residues are known to bind Fe(III) and represent the end point of the calculation.

with the following parametrization were used in this study:

$$\epsilon^{(c)} = 0.6$$

$$\epsilon^{(hb)} = 0.36 \exp[-1.7(R - 2.8)]$$

$$\epsilon^{(ts)} = 0.6 \exp[-1.7(R - 1.4)]$$

The distances, R , are in angstroms and the coupling or decay factors ϵ are unitless. The maximum possible activationless electron-transfer rate constant using Eyring's transition-state theory value of 10^{13} s^{-1} as the upper bound can be estimated from the simple formula:³⁵

$$k_{et} \simeq 1 \times 10^{14} (T'_{DA})^2 \text{ s}^{-1} \quad (1b)$$

The pathway coupling values, T'_{DA} , were calculated using the software HARLEM developed by Igor Kurnikov.^{36,37} This software uses the Dijkstra graph search algorithm to locate the strongest pathway, the set of bonds and through-space interactions that maximize the coupling between donor and acceptor.

In Dutton's average packing density model the electron transfer is assumed to occur via tunneling and the rate falls off exponentially with distance between donor and acceptor while being modulated by the intervening protein. The electron-transfer coupling in this method increases if the packing density of the medium between the donor and acceptor is high. The relationship between the packing density and rate constant is

$$\log_{10} k_{et}^{\text{ex}} = 13.0 - (1.2 - 0.8\rho)(R - 3.6) - 3.1(\Delta G + \lambda)^2/\lambda \quad (2)$$

where R is the edge–edge distance between the donor and acceptor, ρ the packing density between donor and acceptor, ΔG the driving force of the reaction, and λ the reorganization energy. In this model, the path for the electron transfer is the straight line connecting the donor and acceptor. The packing density values and edge–edge distances between donor and acceptor for Dutton's average packing density model were also obtained using the software package HARLEM, and sub-

sequently used to calculate ET rate constants using eq 2 for the activationless case.

In order to explore the effectiveness of electron transfer from the docked flavin ligands RBFH2 and FMNH2, probable acceptor sites within the cavity were first identified. We chose acceptor sites based on two criteria: (1) proximity of the cavity residues to the exterior bound reducing agent, and (2) prior experimental evidence indicating the interior residues bind Fe(III) or are involved in core formation. The terminal sites for electron transfer chosen within the protein coat and on the inner surface of HuHF are all presumed to bind Fe(III). The iron atoms presumed to bind to these sites, the actual acceptors in the electron-transfer step, were not included in the calculations but should reduce the ET coupling, according to the pathways method, by a factor of 0.6. In HuLF, glutamate residues considered to be potential nucleation sites for the mineral core were chosen as the terminal acceptors. In 1BCF, the heme group within the protein is indicated as a possible mediator in the reduction of the mineral core and is considered the electron acceptor in this study. The flavins are known to transfer two electrons in two sequential single electron-transfer steps to acceptors. In all cases, electron-transfer coupling and maximum possible rate constant for transfer of a single electron from the N5 position^{38,39} of the isoalloxazine moiety of RBFH2 and FMNH2 to the different sites within the protein shell were calculated.

IV.B. ET to HuHF. The three sites chosen within the protein shell of HuHF, viz., GLU-27, GLU-62, and GLU-61, represent possible routes to the mineral core. In the case of HuHF, GLU-27 and GLU-62 form part of the ferroxidase center and could be a conduit for ET from the exterior to the nucleation centers and are not located within the cavity. GLU-61 is understood to take part in iron mineralization as a nucleation site and could represent an actual point of contact with the mineral core.⁵ GLU-64 and GLU-67 were also studied as potential mediators.

The pathways coupling (eq 1a) and the rate constants for electron transfer (eq 1b) are given in Table 4 and were calculated for the crystal structure and at different snapshots in time along the MD simulation. Average packing density, donor–acceptor edge–edge distance, and maximum ET rate constants using the average packing density model (eq 2) are

Table 5. Packing Density, ρ , Edge–Edge Distance, and Rate Constants, Using the Average Packing Density Method, Eq 2, for Electron Transfer from RBFH2 and FMNH2 Docked on the Crystal Structure of HuHF and Configurations at Different Time Steps of the MD Simulation^a

terminal glutamate	snapshot (ns)	RBFH2			FMNH2		
		ρ	R (Å)	rate const k_{et} (s^{-1})	ρ	R (Å)	rate const k_{et} (s^{-1})
GLU-27	crystal	0.48	9.2	2.8×10^8	0.18	12.3	6.2×10^3
GLU-61	crystal	0.28	19.4	3.4×10^{-3}	0.68	20.5	9.0×10^0
GLU-62	crystal	0.45	11.3	3.2×10^6	0.45	13.6	3.8×10^4
GLU-27	8.6	1.00	5.5	1.6×10^{12}	1.00	5.5	1.7×10^{12}
GLU-61	8.6	0.48	14.8	7.9×10^3	0.48	14.8	7.9×10^3
GLU-62	8.6	0.25	5.2	2.6×10^{11}	0.25	5.2	2.6×10^{11}
GLU-27	126	1.00	5.2	2.3×10^{12}	1.00	5.3	2.0×10^{12}
GLU-61	126	0.57	14.5	7.7×10^4	0.60	14.4	1.7×10^5
GLU-62	126	0.09	5.5	6.7×10^{10}	0.09	5.4	9.7×10^{10}
GLU-27	156	1.00	5.4	2.0×10^{12}	1.00	5.5	1.8×10^{12}
GLU-61	156	0.64	14.2	4.9×10^5	0.64	14.2	5.0×10^5
GLU-62	156	0.09	5.5	7.2×10^{10}	0.09	5.5	7.3×10^{10}
GLU-27	216	1.00	2.8	1.0×10^{13}	1.00	2.8	1.0×10^{13}
GLU-61	216	0.06	13.4	4.4×10^1	0.22	13.5	6.4×10^2
GLU-62	216	0.00	5.6	3.6×10^{10}	0.00	5.7	2.8×10^{10}

^aThe terminal glutamate residues are known to bind Fe(III) and represent the end point of the calculation.

Table 6. Electron-Transfer Pathways from RBFH2 and FMNH2 Docked on HuHF

HuHF		RBFH2	FMNH2
terminal GLU	snapshot (ns)	ET pathway	ET pathway
GLU-61	crystal	RBFH2-N5 → LEU26 → GLU27 → GLU62 → GLU61 OE2	FMNH2-N5 → TYR29 → ALA30 → SER31 → GLU62 → GLU61 OE2
GLU-62	crystal	RBFH2-N5 → LEU26 → GLU27 → GLU62 OE2	FMNH2-N5 → LEU106 → GLU107 → GLU62 OE2
GLU-27	crystal	RBFH2-N5 → LEU26 → GLU27 OE2 2	FMNH2-N5 → LEU26 → GLU27 OE2
GLU-61	8.6	RBFH2-N5 → GLU-62 → GLU-61 OE2	FMNH2-N5 → GLU-62 → GLU-61 OE2
GLU-62	8.6	RBFH2-N5 → C4A → C4 → O4 (nonbonded jump) GLU-62 OE2	FMNH2-N5 → C4A → C4 → O4 (nonbonded jump) GLU-62 OE2
GLU-27	8.6	RBFH2-N5 → C4A → C4 → N3 (nonbonded jump) GLU-27 OE2	FMNH2-N5 → C4A → C4 → N3 (nonbonded jump) GLU-27 OE2
GLU-61	216	RBFH2-N5 → GLU-27 → GLU-62 → GLU-61 OE2	FMNH2-N5 → GLU-27 → GLU-62 → GLU-61 OE2
GLU-62	216	RBFH2-N5 (nonbonded jump) GLU-27 OE2 → GLU-62 OE1	FMNH2-N5 (nonbonded jump) GLU-27 OE1 → GLU-62 OE2
GLU-27	216	RBFH2-N5 (nonbonded jump) GLU-27 OE2	FMNH2 N5 (nonbonded jump) GLU-27 OE2

given in Table 5. The donor atom is the flavin N5 of the isoalloxazine group and the acceptor is an oxygen atom on the carboxylate group of the relevant glutamate residue. The maximum possible rate constant for electron transfer between RBFH2 and GLU-27 and GLU-62 of the crystal structure is 4.0×10^5 and $9.6 \times 10^2 \text{ s}^{-1}$, respectively, as determined by the pathway model, eqs 1a and 1b (Table 4). The rate constant for transfer from FMNH2 to GLU-27 and GLU-62 following the pathways model is 1.9×10^5 and $2.2 \times 10^2 \text{ s}^{-1}$, respectively. The rate constants determined by the packing density method, Table 5, are higher for RBFH2, at 2.8×10^8 and $3.2 \times 10^6 \text{ s}^{-1}$, respectively (Table 5). The rate constant for electron transfer to GLU-61 is predicted to be much lower by both methods. The pathways model predicts similar values for both flavins: $(1.0\text{--}1.9) \times 10^{-1} \text{ s}^{-1}$.

The pathways of electron transfer at the residue level in the crystal structure is given in Table 6 and pictorially depicted in Figures 20, 21, and 22. The individual bonds involved in the pathway are highlighted in the figures. The electron-transfer pathways to GLU-62 and GLU-61 from FMNH2 are different from that in RBFH2 due to the different orientations of the docked structures. The pathway from RBFH2 is more direct with only LEU-26 as the intermediary. As seen in Figures 20

and 21, transfer from FMNH2 involves many different residues. Multiple through-bond and through-space jumps lead to the slow maximum possible electron-transfer rate constant for transfer to GLU-61.

The average density ET model in eq 2 is sensitive to the packing density, ρ , of the intervening medium, which changes significantly in some cases with change in orientation of the donor with respect to the acceptor as seen in ET from RBFH2 and FMNH2 N5 to GLU-61. The edge to edge distance in the two cases is not very different at 19.4 and 20.5 Å, respectively, but the ρ values are 0.28 and 0.68 leading to 1000-fold difference in k_{et} .

For the configuration 8.6 ns along the MD trajectory, the isoalloxazine rings of both RBFH2 and FMNH2 have the same docked conformations. The pathways change compared to the crystal structure. The electron-transfer pathway to GLU-27 and GLU-62 shows direct transfer to the residues from the flavins (Figure 23). Only covalent bond couplings and one through-space jump to the relevant residue are involved. The overall coupling constants for RBFH2-N5 → GLU-27, GLU-61, and GLU-62 electron transfer increase by a factor of 10^5 , 10^5 , and 10^7 , respectively, following the pathways model. The electron transfer to GLU-61 involves only GLU-62 as the intermediary

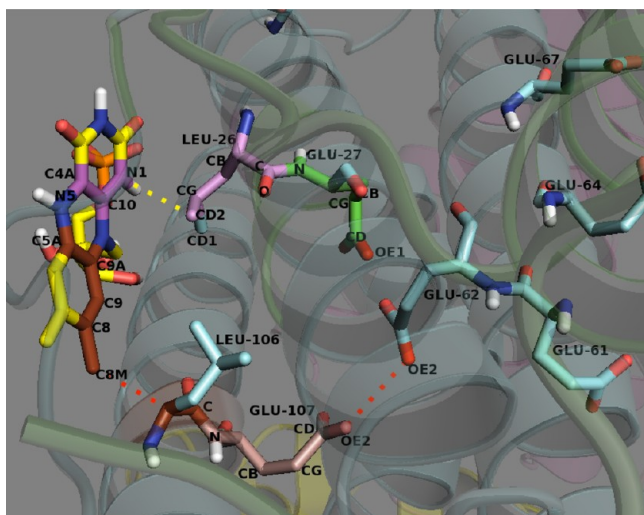


Figure 20. FMNH2 (yellow) docked on the crystal structure of HuHF. The ET path from N5 of FMNH2 to GLU-27 via LEU-26 is highlighted in purple and green. The yellow dashed line indicates a nonbonded jump. The ET path to GLU-62 via LEU-106 and GLU-107 is highlighted in brown and light pink. The nonbonded jumps are highlighted in red.

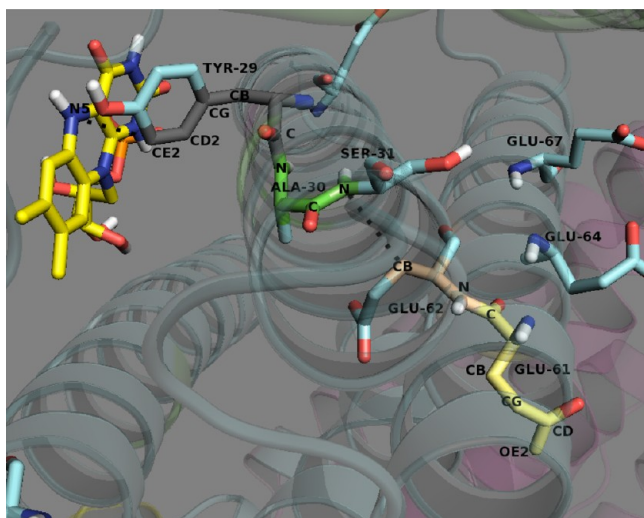


Figure 21. FMNH2 (yellow) docked on the crystal structure of HuHF. The ET path from N5 of FMNH2 to GLU-61 (pale yellow) via TYR-29 (gray), ALA-30 (green), and GLU-62 (light pink). The black dashed lines represent nonbonded jumps.

residue and the rate constant increases to $6.2 \times 10^4 \text{ s}^{-1}$. ET rate constants, calculated using eq 2, show values for transfer to GLU-27 and GLU-62 that are 100-fold higher than seen with the pathways method using eqs 1a and 1b. The edge–edge distances drop by $\sim 5 \text{ \AA}$. The change in rate constants for GLU-27 and GLU-62 is greater for FMNH2 as the edge–edge distances decrease by about 7–8 \AA . The ET rate constant to GLU-61 increases by 4 orders of magnitude as the edge–edge distance decreases from 20.5 to 14.8 \AA .

The electron-transfer coupling constants and pathways do not change much for the different snapshots along the MD simulation trajectory until about 216 ns. The ET rate constants for transfer to GLU-27 and GLU-62 increase by a factor of 10. The electron-transfer pathway is the same for RBFH2 and FMNH2 (Figure 24). A direct nonbonded jump to the terminal

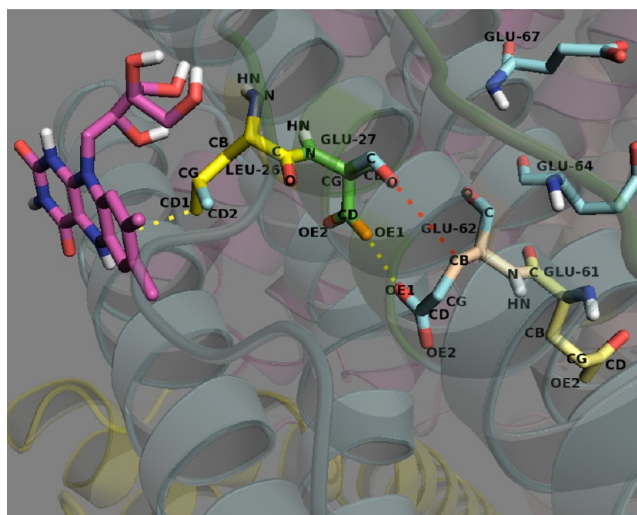


Figure 22. Electron transfer from RBFH2 (pink) docked on the crystal structure of HuHF. The ET path from N5 to GLU-27 OE2 via LEU-26 is highlighted in yellow and green. The yellow dashed line indicates a nonbonded jump from N5 of RBFH2. The path continues to GLU-62 OE1 via a nonbonded jump. The path to GLU-61 via LEU-26, GLU-27 and GLU-62 is highlighted in yellow, green, light pink and wheat and a nonbonded jump (red dashes).

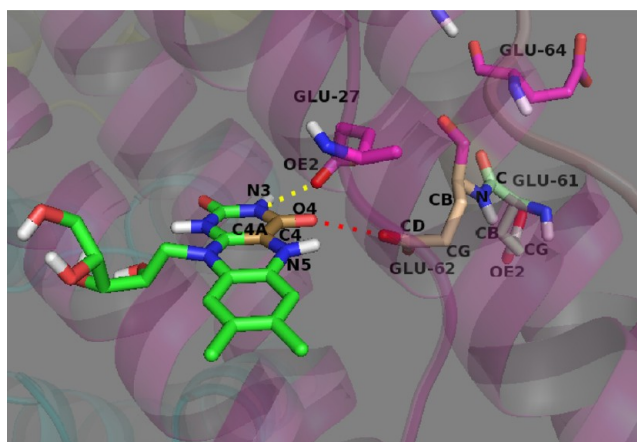


Figure 23. Electron transfer from RBFH2 (green), docked on HuHF (8.6 ns snapshot), to GLU-27, GLU-62, and GLU-61. The atoms involved in the ET path to GLU-27 and GLU-62 are highlighted in brown. The dashed lines represent nonbonded jumps. GLU-62 (pale pink) mediates ET to GLU-61 (light green) OE2.

atom in GLU-27, OE1, is observed as the RBFH2 and FMNH2 donor N5 site is hydrogen bonded to GLU-27. ET to both GLU-61 and GLU-62 is mediated by GLU-27. The donor–acceptor edge–edge distance between the isoalloxazine N5 and GLU-61 decreases to 13.5 \AA but the lower ρ values result in a lower ET rate constant following the packing density model, eq 2. The rate constant for transfer to GLU-27 reaches the maximum value because of the low edge–edge distance. Thus, over a period of 216 ns, the pathway couplings and hence the maximum possible rate constants increase following both the pathway model in eqs 1a and 1b as well as the packing density model, eq 2. The ET rate constants fluctuate to some extent in the case of GLU-62 and GLU-61.

While the electron-transfer rate constants increase dramatically with simulation time, the protein–flavin inhibition constants increase from the 0.1 mM range to up to 4 mM.

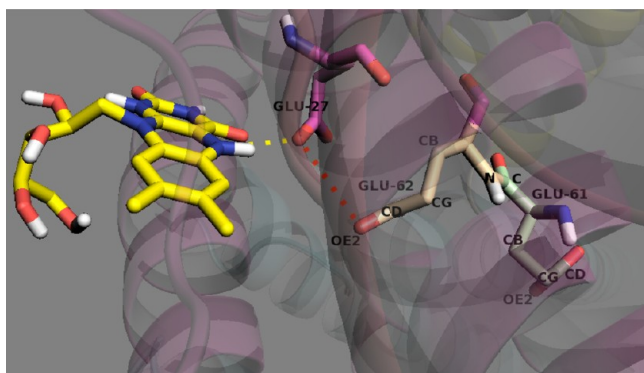


Figure 24. Electron transfer from RBFH2 (yellow), docked on HuHF (216 ns snapshot), to GLU-27, GLU-62, and GLU-61. ET to GLU-27 via one nonbonded jump (yellow dashes) followed by a second nonbonded jump to GLU-62 (red dashes). The path continues to GLU-61 OE2 and is highlighted in wheat and pale green.

From all the experimental evidence available to date, the inhibition constants for flavin binding to ferritin must fall in the millimolar range or more. Ball-park estimates of the ligand residence times can be calculated if the formation of the ligand–protein complex is assumed to be diffusion controlled—the association rate constant would be of the order of $10^7 \text{ M}^{-1} \text{ s}^{-1}$.^{40–42} Using a value of 1 mM for the ferritin–riboflavin inhibition constant, the dissociation rate constant would be of the order of 10^4 s^{-1} . This would give a residence time of the order of 10^{-4} s . Even though the ligand residence times are short, reduction across the protein coat should be efficient as the electron-transfer rate constants for transfer to both GLU-27 and GLU-62 determined far exceed the dissociation rate constants while the rate constant for transfer to GLU-61 is comparable on average to the flavin dissociation rate constants.

ET to the terminal residues GLU-64 and GLU-67 which face the interior of the cavity was also studied for completeness. The ET rate constants are of the order of 10^{-2} for transfer from both RBFH2 and FMNH2 docked on the crystal structure using the pathways method (eqs 1a,1b). The rate constants increase to $\sim 10^2 \text{ s}^{-1}$ for the HuHF configuration at 216 ns for both residues. The ET pathway to GLU-67 at 216 ns is

mediated by GLU-27 and ALA-66. The pathway to GLU-64 is mediated by GLU-27 and HIS-65. The rate constants following the packing density method (eq 2) are higher and range from $\sim 10^2 \text{ s}^{-1}$ for ET from the flavins docked on the crystal structure to $\sim 10^4 \text{ s}^{-1}$ at snapshots along the MD trajectory. In the crystal structure, the distance between the donor N5 position and the terminal oxygen atom of the glutamate residues GLU-64 and GLU-67 is $\sim 20 \text{ \AA}$ and decreases to $\sim 16.5 \text{ \AA}$ over time. The packing density is high and of the order of 0.7.

IV.C. ET to HuLF. The pathway couplings, T'_{DA} , eq 1a, and rate constants, eq 1b, to the nucleation sites GLU-57, GLU-60, GLU-61, and GLU-64 within HuLF are given in Table 7. The packing density, donor–acceptor edge–edge distance, and rate constants following the eq 2 are given in Table 8.

The rate constants for ET to all four glutamates from both FMNH2 and RBFH2 docked on the crystal structure are low according to the pathways model, eqs 1a and 1b. The pathways model shows a modest change in rate constants compared to the crystal structure within the simulation time frame of 20 ns. The rate constants show a 10-fold increase at 20 ns and are of the order of 10^1 s^{-1} . The pathway to GLU-61 in HuLF at 20 ns is given Table 9 and depicted in Figure 25. The individual bonds involved in the pathway are highlighted in the figure. The salt bridge between LYS-62 and GLU-107 which is observed in the crystal structure adds rigidity to the helix bundle and persists along the simulation trajectory and is shown in the figure. The location of the cavity is similar for the configurations at 10 and 20 ns. The docking orientation of the flavins shows the isoalloxazine ring oriented toward the helices and not the interior of the cavity. The pathway of electron transfer is mediated by the residues ALA-30 and LYS-62 via two through-space jumps which results in the low pathways coupling.

The rate constants to GLU-60, GLU-61, and GLU-64 increase considerably for configurations along the MD trajectory using eq 2. The rate constant for ET to GLU-61 in particular goes from $\sim 10^2$ to $\sim 10^6 \text{ s}^{-1}$. The edge–edge distance decreases to $\sim 15.0 \text{ \AA}$ at 10 ns and $\sim 17.0 \text{ \AA}$ at 20 ns. The packing density increases to ~ 0.8 for the configurations at 10 and 20 ns and can be explained by the orientation of the isoalloxazine ring (Figure 25). Both the decreased edge–edge

Table 7. Pathway Coupling, T'_{DA} , Eq 1a, and Rate Constants, Eq 1b, for Electron Transfer from RBFH2 and FMNH2 Docked on the Crystal Structure of HuLF and Configurations at Different Time Steps of the MD Simulation^a

terminal glutamate	snapshot (ns)	RBFH2		FMNH2	
		T'_{DA}	rate const k_{et} (s^{-1})	T'_{DA}	rate const k_{et} (s^{-1})
GLU-57	crystal	1.0×10^{-7}	1.0×10^0	4.8×10^{-8}	2.3×10^{-1}
GLU-60	crystal	2.6×10^{-7}	6.8×10^0	1.2×10^{-7}	1.4×10^0
GLU-61	crystal	5.6×10^{-8}	3.1×10^{-1}	2.7×10^{-8}	7.3×10^{-2}
GLU-64	crystal	1.1×10^{-8}	1.2×10^{-2}	5.2×10^{-9}	2.7×10^{-3}
GLU-57	10	6.7×10^{-8}	4.5×10^{-1}	8.3×10^{-8}	6.9×10^{-1}
GLU-60	10	3.0×10^{-7}	9.0×10^0	3.7×10^{-7}	1.4×10^1
GLU-61	10	9.4×10^{-8}	8.8×10^{-1}	2.3×10^{-7}	5.3×10^0
GLU-64	10	7.5×10^{-8}	5.6×10^{-1}	1.1×10^{-7}	1.2×10^0
GLU-57	20	4.4×10^{-7}	2.0×10^1	4.8×10^{-7}	2.3×10^1
GLU-60	20	4.9×10^{-7}	2.4×10^1	5.5×10^{-7}	3.0×10^1
GLU-61	20	2.8×10^{-7}	7.8×10^0	2.7×10^{-7}	7.3×10^0
GLU-64	20	6.0×10^{-8}	3.6×10^{-1}	5.9×10^{-8}	3.5×10^{-1}

^aThe terminal glutamate residues are presumed nucleation sites for ferrihydrite formation within the ferritin cavity and represent the end point of the calculation.

Table 8. Packing Density, ρ , Edge–Edge Distance, and Rate Constants Using the Average Packing Density Method, Eq 2, for Electron Transfer from RBFH2 and FMNH2 Docked on the Crystal Structure of HuLF and Configurations at Different Time Steps of the MD Simulation^a

terminal glutamate	snapshot (ns)	RBFH2			FMNH2		
		ρ	R (Å)	rate const k_{et} (s^{-1})	ρ	R (Å)	rate const k_{et} (s^{-1})
GLU-57	crystal	0.82	20.6	6.3×10^3	0.52	20.7	3.1×10^{-1}
GLU-60	crystal	0.74	21.6	1.2×10^2	0.68	21.1	3.7×10^1
GLU-61	crystal	0.61	18.6	2.0×10^2	0.57	19.9	7.0×10^0
GLU-64	crystal	0.71	21.1	6.6×10^1	0.61	22.3	5.7×10^{-1}
GLU-57	10	0.79	20.5	2.2×10^3	0.69	20.3	1.7×10^2
GLU-60	10	0.76	19.3	5.7×10^3	0.71	19.1	1.8×10^3
GLU-61	10	0.81	15.1	4.7×10^6	0.83	14.8	9.4×10^6
GLU-64	10	0.84	20.0	2.1×10^4	0.83	19.8	2.1×10^4
GLU-57	20	0.64	19.3	1.5×10^2	0.64	19.2	1.8×10^2
GLU-60	20	0.74	18.6	7.2×10^3	0.68	17.8	4.9×10^3
GLU-61	20	0.87	17.3	1.1×10^6	0.87	17.4	1.1×10^6
GLU-64	20	0.85	19.1	8.9×10^4	0.82	19.0	3.8×10^4

^aThe terminal glutamate residues are presumed nucleation sites for ferrihydrite formation within the ferritin cavity and represent the end point of the calculation.

Table 9. Electron-Transfer Pathways from RBFH2 and FMNH2 Docked on HuLF and 1BCF

HuLF		RBFH2
terminal GLU	snapshot	ET pathway
GLU-61	20 ns	RBFH2 N5 → ALA-30 → LYS-62 → GLU-61
1BCF		
HEM-204 CBB	crystal	RBFH2-N5 → VAL-20 → LEU-19 → HEM-204 CBB

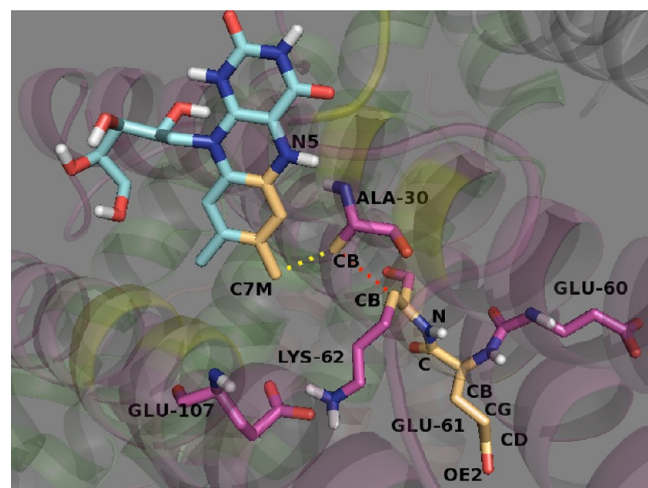


Figure 25. Electron transfer from RBFH2 (blue), docked on HuLF (20 ns snapshot), to GLU-61 via ALA-30 and LYS-62. The atoms involved in the ET path are highlighted in wheat. The dashed lines represent nonbonded jumps. GLU-107 and LYS-62 form a salt bridge.

distance and increased packing density contribute to the enhanced rate constants along the MD trajectory.

IV.D. ET to 1BCF. The bacterial ferritin 1BCF shows an interesting variation as it has a heme at each 2-fold symmetry site inside the ferritin cavity. Electron transfer from the flavins docked in the three pockets identified in section III.C (Figure 3a) was studied. These three sites, from visual inspection of the molecular surface, appear to be possible routes for electron transfer to heme. Results for ET from RBFH2 and FMNH2 docked onto the crystal structure are given in Tables 10 and 11.

Two acceptor sites were used, the Fe atom of the heme as well as the edge of the heme (Figure 26). Some ET studies have shown⁴³ that the electron-transfer rate constants derived using a donor–acceptor edge–edge distance based on the edge of the heme macrocycle give better results than using donor–Fe distances. We chose the edge of the heme to be the CBB atom of the ethenyl moiety (vinyl substituent) in this paper as it is closer to the pockets on the surface of 1BCF and there is also evidence of conjugation of the vinyl group with the heme macrocycle.⁴⁴ The electron-transfer rate constant for transfer from the flavins docked at pocket 3 is significant and of the order of 10^6 s^{-1} to the heme edge using eq 2. The electron-transfer rate constants for transfer to Fe and heme edge are lower when the flavins are docked at pockets 1 and 2.

The pathway model using eqs 1a and 1b yields lower values, but still of the order of 10^2 s^{-1} for ET to vinyl-CBB. The pathway to the ethenyl substituent of heme from the N5 position of both RBFH2 and FMNH2 docked in pocket 3 is the same and is shown in Table 9 and in Figure 26. The covalent bonds involved in the path are labeled and shown in the figure. VAL-20 and LEU-19 are seen to mediate ET to vinyl-CBB. The pathway to Fe is mediated by VAL-20, LEU-19, and vinyl-CBB. Individual bonds involved are highlighted in different colors in the figure.

As the edge to edge distance and the path length to the Fe atom are greater than to the vinyl group, both ET methods give lower values of the ET rate constants to Fe. ET rate constants using eqs 1b and 2 do not give identical results and in some cases show orders of magnitude difference in electron-transfer rate constants. This has been observed in other studies^{45,46} especially when donor or acceptor involved a macrocycle like heme.

V. CONCLUSIONS

We have used a combination of computational modeling methods to study docking of redox agents and subsequent electron transfer through the protein coat of several ferritin structures. Experimental measurements to determine the mechanism of these processes on the molecular level is difficult. Molecular dynamics simulations have allowed us to sample ferritin conformations in solution. Docking studies and electron-transfer calculations have enabled us to study how

Table 10. Pathway Coupling, T'_{DA} , Eq 1a, and Rate Constants, Eq 1b, for Electron Transfer from RBFH2 and FMNH2 Docked on the Crystal Structure of 1BCF^a

terminal site	pocket	RBFH2		FMNH2	
		T'_{DA}	rate const k_{et} (s^{-1})	T'_{DA}	rate const k_{et} (s^{-1})
Fe	pocket 1	8.9×10^{-8}	7.9×10^{-1}	7.3×10^{-8}	5.2×10^{-1}
Fe	pocket 2	7.3×10^{-8}	5.1×10^{-1}	3.1×10^{-7}	9.6×10^0
Fe	pocket 3	1.2×10^{-7}	1.4×10^0	7.8×10^{-8}	6.1×10^{-1}
vinyl-CBB	pocket 1	1.1×10^{-6}	1.2×10^2	9.3×10^{-7}	8.7×10^1
vinyl-CBB	pocket 2	5.0×10^{-7}	2.5×10^1	4.0×10^{-6}	1.6×10^3
vinyl-CBB	pocket 3	1.5×10^{-6}	2.3×10^2	5.1×10^{-7}	2.6×10^1

^aThe vinyl moiety of the heme as well as the Fe center represent acceptor sites. The flavin N5 site was considered the donor.

Table 11. Packing Density, ρ , Edge–Edge Distance, and Rate Constants Following the Average Packing Density Method, Eq 2, for Electron Transfer from RBFH2 and FMNH2 Docked on the Crystal Structure of 1BCF^a

terminal site	pocket	RBFH2			FMNH2		
		ρ	R (Å)	rate const k_{et} (s^{-1})	ρ	R (Å)	rate const k_{et} (s^{-1})
Fe	pocket 1	0.51	22.4	1.3×10^{-2}	0.41	20.2	3.4×10^{-2}
Fe	pocket 2	0.36	19.9	1.2×10^{-2}	0.41	19.7	8.7×10^{-2}
Fe	pocket 3	0.73	18.9	4.2×10^3	0.70	19.5	6.5×10^2
vinyl-CBB	pocket 1	0.68	16.0	7.0×10^4	0.06	14.1	7.7×10^0
vinyl-CBB	pocket 2	0.13	15.9	3.1×10^{-1}	0.35	14.0	2.9×10^3
vinyl-CBB	pocket 3	0.88	15.9	7.7×10^6	0.85	16.5	1.7×10^6

^aThe vinyl moiety of the heme as well as the Fe center represent the acceptor sites. The flavin N5 site was considered the donor.

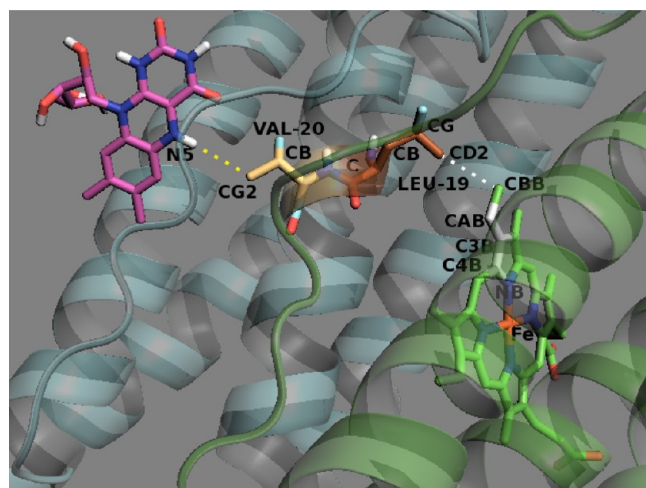


Figure 26. Electron transfer from RBFH2 (pink) docked on pocket 3 within the 4-helix bundle of 1BCF to HEME (green). The path followed via VAL-20 (wheat) and LEU-19 (brown) is highlighted. The yellow dashes represent nonbonded jumps. The path from CBB to the Fe atom is indicated in white. The participating nitrogen atoms are named and colored blue.

flavin molecules bind to the protein surface and to estimate mechanisms and rate constants for electron transfer across the protein coat.

The docking results show that, in all the ferritins studied, the inhibition constants for flavin binding are high (of the order of a few mM) especially for configurations taken a few nanoseconds along a MD simulation trajectory. This is in keeping with the experimental observation that no stable complex of 1 mM or less has been isolated using equilibrium dialysis to date. A rapid equilibrium would ensure quick release of the reductant subsequent to electron transfer across the protein coat. Backbone and side-chain motion is found to have a significant effect on binding. The nature of the ligand binding

pockets changes dramatically for different protein configurations sampled along the MD trajectory, especially in the case of HuHF, with the GLU-27 and GLU-62 moving closer to the pocket surface. The docked conformations in HuHF adopt a more favorable orientation for ET across the protein coat after simulation for a few nanoseconds compared to the crystal structure. Of the two reductants chosen for this study, RBFH2 has a polar ribose side chain and FMNH2 has a charged side chain due to the phosphate group. In all the cases FMNH2 binding is seen to be associated with a basic residue, either lysine or arginine, within the pocket on the protein surface. The ribose moiety of RBFH2 shows more variation in binding as it is not always associated with a basic residue.

Both the docking studies and the electron-transfer computations show that there are strong structure–function relationships between the ferritin conformation and observed docking sites and electron-transfer kinetics. In the case of HuHF the rate constants for ET to GLU-27 and GLU-62 increased dramatically for configurations along a MD simulation trajectory. The rate constant for the nucleation site GLU-61 was also found to be considerable. The maximum possible electron-transfer rate constants to the nucleation site GLU-61 calculated following the packing density model, eq 2, is found to vary from $\sim 10^{-3} s^{-1}$ in the crystal structure up to $\sim 10^5 s^{-1}$ for configurations along the MD simulation trajectory. The ET rate constants calculated by the pathways method using eq 1b vary from $\sim 10^{-1}$ up to $\sim 10^4 s^{-1}$. ET to GLU-64 and GLU-67 is predicted to be a factor of 10 slower than ET to GLU-61; however, these may also play a role in core reduction mediated by the protein coat.

These two different ET models (eqs 1a, 1b and 2) have yielded interesting results for ET rate constants for transfer across the ferritin protein shell. In general, both methods show the same trends, and both methods yield self-consistent results for all the configurations we have studied. As shown in the tables, the two methods yield rate constants that may differ by several orders of magnitude from each other. This has been

observed in other comparative studies for a wide range of proteins.⁴⁵ As noted, the pathways model using eqs 1a and 1b, and Dutton's average density model using eq 2, weight through-space interactions differently. In the ferritin studies, the rate constants estimated by the average density model are consistently higher than those estimated by the pathways model. As noted by Jones et al.,⁴⁵ using the parametrization of the models in this paper, ET rate constants calculated using the pathways model will yield values that are consistently smaller if there is significant through-space tunneling between the donor and the acceptor. In general, it is difficult to determine the electron-transfer rate constants accurately using computational models so as to guarantee exact agreement between experiment and theory.

ET rate constants for transfer to the presumed nucleation sites in HuLF are not uniformly high. The transfer to GLU-61 is rapid as calculated by the average density ET model in eq 2, especially for protein configurations sampled along the MD trajectory. The rate constant does not change along the MD trajectory using the pathways model. We attribute this to the more rigid framework of the 4-helix bundle in HuLF. In 1BCF one of the binding sites, pocket 3, appears to be a good candidate for ET to the heme. It would be interesting in future studies to examine how ET kinetics in 1BCF is altered by ferritin motion.

Using a computational approach, we have been able to determine the feasibility of protein-mediated reductive release of iron from ferritins. Our simulation models have provided insight into how different protein configurations sampled in the solvent phase affects structure/function relationships in ferritins. This study has provided an all-atom view of potential mechanisms for the key processes involved in the release of iron from ferritin. It is expected that the suggested mechanisms for electron transfer, computed binding constants, and electron-transfer rate constants will be used to guide future experiments and studies to further elucidate the mechanisms of the key processes at the molecular level.

AUTHOR INFORMATION

Corresponding Author

*E-mail: debi@unm.edu.

Notes

The authors declare no competing financial interest.

ACKNOWLEDGMENTS

D.G.E. is a Cottrell Scholar of the Research Corp. and a Camille Dreyfus Teacher-Scholar. This project was supported by the Nanoscience and Microsystems Program and the Department of Chemistry and Chemical Biology, University of New Mexico. This work was partially supported by a grant from the Petroleum Research Fund (PRF no. 43207-AC10) administered by the ACS. This research was supported by an allocation of advanced computing resources (project no. CHEO90005) provided by the National Science Foundation. The computations were performed on Kraken at the National Institute for Computational Sciences. We thank Dr. Ilya Balabin for the support provided for the pathways VMD plugin.

REFERENCES

- (1) Harrison, P. M. *Biochim. Biophys. Acta, Bioenerg.* **1996**, *1275*, 161–203.
- (2) Arosio, P.; Ingrassia, R.; Cavadini, P. *Biochim. Biophys. Acta* **2009**, *1790*, 589–99.
- (3) Theil, E. C. *J. Nutr.* **2003**, *133*, 1549S–1553S.
- (4) Chasteen, N. D.; Harrison, P. M. *J. Struct. Biol.* **1999**, *126*, 182–94.
- (5) Hempstead, P. D.; Yewdall, S. J.; Fernie, A. R.; Lawson, D. M.; Artymiuk, P. J.; Rice, D. W.; Ford, G. C.; Harrison, P. M. *J. Mol. Biol.* **1997**, *268*, 424–48.
- (6) Lawson, D. M.; Treffry, A.; Artymiuk, P. J.; Harrison, P. M.; Yewdall, S. J.; Luzzago, A.; Cesareni, G.; Levi, S.; Arosio, P. *FEBS Lett.* **1989**, *254*, 207–10.
- (7) Frolov, F.; Kalb Gilboa, A. J.; Yariv, J. *Nat. Struct. Biol.* **1994**, *1*, 453–460.
- (8) Moore, G. R.; Kadir, F. H.; Al-Massad, F. *J. Inorg. Biochem.* **1992**, *47*, 175–81.
- (9) Moënne-Loccoz, P.; Krebs, C.; Herlihy, K.; Edmondson, D. E.; Theil, E. C.; Huynh, B. H.; Loehr, T. M. *Biochemistry* **1999**, *38*, 5290–5.
- (10) Brady, M. C.; Lilley, K. S.; Treffry, A.; Harrison, P. M.; Hider, R. C.; Taylor, P. D. *J. Inorg. Biochem.* **1989**, *35*, 9–22.
- (11) Gálvez, N.; Ruiz, B.; Cuesta, R.; Colacio, E.; Domínguez-Vera, J. M. *Inorg. Chem.* **2005**, *44*, 2706–9.
- (12) Liu, X.; Jin, W.; Theil, E. C. *Proc. Natl. Acad. Sci. U.S.A.* **2003**, *100*, 3653–8.
- (13) Takagi, H.; Shi, D.; Ha, Y.; Allevell, N. M.; Theil, E. C. *J. Biol. Chem.* **1998**, *273*, 18685–8.
- (14) Liu, X. S.; Patterson, L. D.; Miller, M. J.; Theil, E. C. *J. Biol. Chem.* **2007**, *282*, 31821–5.
- (15) Kidane, T. Z.; Sauble, E.; Linder, M. C. *Am. J. Physiol. Cell Physiol.* **2006**, *291*, C445–C455.
- (16) Sirivech, S.; Frieden, E.; Osaki, S. *Biochem. J.* **1974**, *143*, 311–5.
- (17) Watt, G. D.; Jacobs, D.; Frankel, R. B. *Proc. Natl. Acad. Sci. U.S.A.* **1988**, *85*, 7457–61.
- (18) Jones, T.; Spencer, R.; Walsh, C. *Biochemistry* **1978**, *17*, 4011–7.
- (19) Yang, X.; Arosio, P.; Chasteen, N. D. *Biophys. J.* **2000**, *78*, 2049–59.
- (20) Beratan, D. N.; Onuchic, J. N.; Winkler, J. R.; Gray, H. B. *Science (New York, N.Y.)* **1992**, *258*, 1740–1.
- (21) Page, C. C.; Moser, C. C.; Chen, X.; Dutton, P. L. *Nature* **1999**, *402*, 47–52.
- (22) Berendsen, H.; van der Spoel, D.; van Drunen, R. *Comput. Phys. Commun.* **1995**, *91*, 43–56.
- (23) Lindahl, E.; Hess, B. *J. Mol. Model.* **2001**, *7*, 306–317.
- (24) van Gunsteren, W. F.; Billeter, S. R.; Eising, A. A.; Hunenberger, P. H.; Kruger, P.; Mark, A. E.; Scott, W. R. P.; Tironi, I. G. *Biomolecular Simulation: The GROMOS96 Manual and User Guide*; Hochschulverlag AG an der ETH Zurich: Zurich, Switzerland, 1996.
- (25) Branden, C.; Tooze, J. *Introduction to Protein Structure*; Garland Publishing, Inc.: New York, 1999.
- (26) The PyMOL Molecular Graphics System, version 1.5, Schrodinger, LLC.
- (27) Dundas, J.; Ouyang, Z.; Tseng, J.; Binkowski, A.; Turpaz, Y.; Liang, J. *Nucleic Acids Res.* **2006**, *34*, W116–8.
- (28) Kleywegt, G. J.; Jones, T. A. *Acta Crystallogr.* **1998**, *D54*, 1119–1131.
- (29) Morris, G. M.; Goodsell, D. S.; Halliday, R. S.; Huey, R.; Hart, W. E.; Belew, R. K.; Olson, A. J. *J. Comput. Chem.* **1998**, *19*, 1639–1662.
- (30) Huey, R.; Morris, G. M.; Olson, A. J.; Goodsell, D. S. *J. Comput. Chem.* **2007**, *28*, 1145–1152.
- (31) Wang, Z. M.; Li, C.; Ellenburg, M. P.; Soistman, E. M.; Ruble, J. R.; Wright, B. S.; Ho, J. X.; Carter, D. C. *Acta Crystallogr., Sect. D* **2006**, *62*, 800–806.
- (32) Yasmin, S.; Andrews, S. C.; Moore, G. R.; Le Brun, N. E. *J. Biol. Chem.* **2011**, *286*, 3473–83.
- (33) Beratan, D. N.; Betts, J. N.; Onuchic, J. N. *Science* **1991**, *252*, 1285–1288.
- (34) Betts, J. N.; Beratan, D. N.; Onuchic, J. N. *J. Am. Chem. Soc.* **1992**, *114*, 4043–4046.
- (35) Tan, M.-L.; Balabin, I.; Onuchic, J. N. *Biophys. J.* **2004**, *86*, 1813–9.

- (36) Kurnikov, I. V. University of Pittsburgh, Pittsburgh, PA, www.kurnikov.org, 2000.
- (37) Balabin, I. A.; Hu, X.; Beratan, D. N. *J. Comput. Chem.* **2012**, *33*, 906–910.
- (38) Dixon, D. A.; Lindner, D. L.; Branchaud, B.; Lipscomb, W. N. *Biochemistry* **1979**, *18*, 5770–5775.
- (39) Nakai, S.; Yoneda, F.; Yamabe, T. *Theor. Chem. Acc.* **1999**, 109–116.
- (40) Meyer, B.; Peters, T. *Angew. Chem., Int. Ed.* **2003**, *42*, 864–890.
- (41) Monasterio, O. *Methods (San Diego, Calif.)* **2001**, *24*, 97–103.
- (42) Fersht, A. *Structure and Mechanism in Protein Science*; W.H. Freeman and Co.: New York, 1999; pp 164–165.
- (43) Moser, C. C.; Chobot, S. E.; Page, C. C.; Dutton, P. L. *Biochim. Biophys. Acta* **2008**, *1777*, 1032–1037.
- (44) Choi, S.; Spiro, T. G.; Langry, K. C.; Smith, K. M. *J. Am. Chem. Soc.* **1982**, *104*, 4337–4344.
- (45) Jones, M. L.; Kurnikov, I. V.; Beratan, D. N. *J. Phys. Chem. A* **2002**, *106*, 2002–2006.
- (46) Beratan, D. N.; Balabin, I. A. *Proc. Natl. Acad. Sci. U.S.A.* **2008**, *105*, 403–4.